Influence of surface energy anisotropy on the dynamics of quantum dot growth

Jean-Noël Aqua*,† and Thomas Frisch*,‡
Institut Matériaux Microélectronique Nanoscience de Provence, Aix-Marseille Université, UMR CNRS 6242, 13997 Marseille, France
(Received 11 May 2010; revised manuscript received 14 July 2010; published 20 August 2010)

We investigate the influence of surface energy anisotropy on the dynamics of quantum dot growth by looking at the long-time dynamics of the morphological (Asaro-Tiller-Grinfeld) instability of a strained thin film driven by surface diffusion during growth and annealing. We derive a continuum model accounting for anisotropic surface energy, wetting, and elastic energies. We obtain a nonlinear nonlocal evolution equation for the film height in the small-slope approximation which we solve numerically given a gamma plot of the surface energy based on experimental properties of silicon-germanium films. A small anisotropy induces a complete change in the coarsening dynamics. The noninterrupted coarsening (Ostwald ripening) at stake for isotropic strained films is destroyed by anisotropy and the system is glued in metastable states. We characterize the statistical properties of the resulting pyramids and show that both their density and mean volume can increase with the total amount of matter. We find an optimal mean film height at which the island size distribution is peaked. These results indicate that different island density or volume may be obtained by varying solely the quantity of matter. Finally, we present an energetic model which describes energetic pathways along which ripening can indeed be suppressed.

DOI: 10.1103/PhysRevB.82.085322 PACS number(s): 81.15.Hi, 68.35.Ct, 81.10.Aj, 47.20.Hw

I. INTRODUCTION

Self-organization of elastically strained nanostructures in the Stranski-Krastanow (SK) growth mode has attracted much attention both as a fundamental research issue but also due to its potential applications for electronic and optoelectronic devices.[1–10] For example, high efficiency quantum dots are under active consideration for laser applications.[11] In the SK mode where a film is coherently deposited on a substrate, islands lying on a wetting layer arise, once the film exceeds a critical thickness above which the flat geometry becomes unstable and relax the elastic stress. This mode is observed in many semiconductors and metallic systems and may be used to grow dislocation free self-organized nanostructures as long as the misfit between the film and substrate is low enough.

The silicon/germanium films serve as a paradigm for the SK growth mode. The balance between anisotropy, wetting, elastic relaxation, alloying and kinetics has revealed a variety of shapes which are still under investigation.[7,9,12–16] It is now well established that there exists two growth regimes for $Si_{1-x}Ge_x$ films deposited on Si(001) depending on the intensity of stresses tuned by x. For x larger than 0.5, the usual nucleation regime is operating and small three-dimensional islands suddenly nucleate at spatially disordered positions after deposition of a critical height. In this regime, the emergence of islands is strongly influenced by microscopic effects (adatom diffusion, attachment/detachment to steps or nuclei, intermixing) and an atomistic view is required to describe the growth or annealing dynamics.[14] On the other hand, for smaller stresses, a nucleationless evolution is observed.[17,18] Above a given critical height, the film becomes unstable and develops undulations[17–24] with a well-defined horizontal wavelength. This elastic instability is the variation in the Asaro-Tiller-Grinfeld (ATG) instability[25,26] which depends on the competition between surface and elastic energies and results from surface diffusion induced by chemical-potential gradients. This scenario leads to modulated patterns (ripples) characterized by a wavelength ranging from 10 to 100 nm depending on the misfit value.[17,18,27–29]

We focus in the present article on the long-time dynamics of this elastic instability and notably on its dependence on anisotropy. Indeed, after the initial stages of the instability characterized by a typical wavelength, islands separated by a wetting layer arise and may coarsen. After some time for coarsening where small prepyramidal islands grow with an increasing aspect ratio and thence increasing slopes, the islands exhibit strong anisotropy as they first display square-base pyramidal shapes[27,28] before evolving into more complex geometries, see, e.g., Ref. 7. Even though kinetic differences between the nucleation and instability regimes exist, the presence of strain-induced (105) facets[17,18,27,28] in Si/Ge systems is accountable[30,31] in both cases for the pyramidal shapes. Hence, we aim at depicting the development of anisotropic islands and their subsequent evolution. Experiments on Si/Ge by Berbezier *et al.*[28,29] revealed that annealing of thin films lead to an evolution frozen in a dense array of pyramids. The resulting islands display a noticeable size dispersion and their positions are not organized on a regular array.

As regards the long-time dynamics of the ATG instability in isotropic systems, one may recall that the competition between surface and elastic energy leads to finite-time singularities which eventually lead to fracture generation in thick films.[23,32–38] In thin films, however, wetting interactions between the film and the substrate may impact the long-time dynamics.[39–42] The nonlinear analysis of the instability in presence of smooth wetting interactions was hence studied in Ref. 41, where the elastic problem was solved under the thin-film hypothesis. It was shown that the nonlocal nonlinear effects are necessary to prevent the finite-time singularity of the instability. The initial instability then lead to a surface where isotropic islands separated by a wetting layer undergo Ostwald ripening, where large islands grow at the expense of small ones due to mass transfer via the wetting layer. The

numerical analysis of the long-time dynamics then reveals[41] a noninterrupted coarsening characterized by an algebraic decay of the number of islands, which exponent depends markedly on the system dimensionality. However, the latter isotropic dynamics is driven by an elastic relaxation which driving force is mainly the increase in the island aspect ratio which relaxes the elastic stress more efficiently. This scenario may hence apply to the first stages of the experimental instability, where the initial corrugation transforms into isotropic prepyramids but not to subsequent stages characterized by anisotropic islands. One may indeed question the influence of the surface energy anisotropy on the driving force of the dynamics. Moreover, the morphology resulting from the different growth modes is of crucial interest and we also aim at characterizing the surface statistical properties, island density, mean island volume, and island size distribution.

It was shown in Ref. 43 on the basis of an energetic model describing an array of pyramidal islands of volume V and density n that an optimum island size exists for a given deposited height *and* given island density. In particular, the optimal island size increases when the island density diminishes.[43] However, the energy of the optimal configuration keeps on decreasing as the island density diminishes at constant amount of matter so that Ostwald ripening is expected in this description. Simulations of the dynamical evolution of these systems then revealed helpful. Large scale numerical simulations of island growth suffers from the inherent difficulty of treating the long-range elastic forces and the geometrical nonlinearity of the stress-free boundary conditions. Despite intrinsic limitations, finite elements (FE) simulations of continuum mechanics models[44–49] have been used to study both growth and annealing in the SK mode and revealed new features. A large mismatch and large wetting potential were shown to lead to islands stable against coarsening in anisotropic films.[44,46] On the other hand, a very small anisotropy (described by variations in the surface energy of relative order 10^{-4}) revealed also a possible interrupted coarsening.[45] In the finite element methods, the strain energy density at the film free surface has to be, in principle, calculated at each time steps and this may impose some limitations on the scale on the system. Despite this difficulty the FE simulations are extendable to large slopes which are commonly found in domes and barn shape and also in prepatterned strained geometries.[50]

Here, we choose to work with an alternative method allowing for large-scale simulations by using the small-slope approximation in which an explicit nonlinear integrodifferential equation for the film height is derived. This framework was introduced in Ref. 35 in order to treat the case of an isotropic film lying on a nondeformable substrate and where the evolution equation leads to finite-time singularities characterized by a slope divergence due to nonlinear local terms. This phenomena can be rationalized in terms of elastic stress concentration and is reminiscent of the ATG finite-time singularities.[25,36,51] An extension of the latter work was done in order to include the deformability of the substrate together with wetting interactions between the film and substrate.[39–41] The combination of both wetting and nonlinear nonlocal elasticity then regularizes the dynamical singularity and leads to a long-time dynamics characterized by islands separated by a wetting layer. During annealing, the film undergoes Ostwald ripening where large islands grow at the expense of smaller ones due to mass transfer through the wetting layer. In isotropic systems, the latter coarsening is noninterrupted[40,41] and the surface tends to its absolute minimum of energy, as corroborated by FE simulations.[52] However, after some time for coarsening, islands display slopes comparable with the first facet angle (which corresponds to the (105) facet in Si/Ge) and anisotropy is crucial for a proper analysis of the subsequent evolution. The small-slope approximation will be all the more justified as pyramids develop angles at most corresponding to the (105) facets, see, e.g., Ref. 17.

In the present Article, we derive a continuum model accounting for anisotropic surface energy, wetting, and elastic interactions and derive the nonlinear evolution equation necessary to investigate the long-time dynamics of the instability. We solve numerically the latter equation using large-scale simulations and discuss the effects of the surface energy anisotropy on ripening during growth and annealing. We show that an interrupted coarsening happens when a plausible surface energy anisotropy and wetting potential are considered. The system is then characterized by a disordered array of islands whose density and volume are functions of the total amount of matter. We find that the island density in the stationary regime increases as function of the deposited height until it reaches a plateau where elastic interactions, steric effects, and shape evolution occur. We find an optimal amount of matter for which the island size distribution is narrow and accordingly, the island size dispersion reduced. In order to understand the origin of the interrupted coarsening of pyramids, we present an energetic model which describes energetic pathways relevant for describing Ostwald ripening where fixed islands exchange matter via surface diffusion. The combination of anisotropy, wetting, and elasticity, enforces the model to display a valley of states with an energy difference, which is the driving force for coarsening, that is vanishingly small.

In Sec. II we present in a self-contained presentation, the ingredients of our continuum model including surface effects (anisotropy and wetting) and elasticity. In Sec. III, we discuss the results of the numerical resolution of the evolution equation derived in Sec. II. In Sec. IV, we generalize the energetic model of Ref. 43 in order to compute energetic pathways relevant for the Ostwald ripening.

II. CONTINUUM MODEL

A. Surface diffusion

We aim at modelizing the elastic instability at stake in semiconductor films[5,17–24,53] when the temperature is high enough to allow surface diffusion but low enough so that volume diffusion together with evaporation can be neglected. Following Mullins,[54] we write mass conservation during surface diffusion induced by surface currents proportional to gradients of the surface chemical potential μ. It enforces the conservation equation[55]

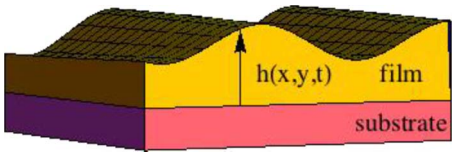

FIG. 1. (Color online) Geometry of the film/substrate system.

$$\partial h/\partial t = F + D\sqrt{1+|\nabla h|^2}\Delta_S \mu, \tag{1}$$

where $h(\boldsymbol{r},t)$ is the free surface of the film with $\boldsymbol{r}=(x,y)$, see Fig. 1, F is the deposition flux, D a diffusion coefficient, Δ_S, the surface Laplacian, and μ is homogeneous to an energy density.

The chemical potential at the surface is defined by the energy difference due to mass variation, which can be computed by functional derivatives[51]

$$\mu = \delta\mathcal{F}/\delta h \tag{2}$$

of the free energy of the system which encompasses surface and elastic contributions $\mathcal{F}=\mathcal{F}^s+\mathcal{F}^{el}$ so that $\mu=\mu^s+\mu^{el}$. The surface energy

$$\mathcal{F}^s = \int \gamma(h,\boldsymbol{n})\sqrt{1+|\nabla h|^2}d\boldsymbol{r} \tag{3}$$

includes both for wetting effects and surface energy anisotropy via, respectively, the dependence of the local surface energy γ on the film height and on the local orientation of the surface described by its normal $\boldsymbol{n}=(-h_x,-h_y,1)/\sqrt{1+|\nabla h|^2}$. The elastic energy is given by the integral over both the film and the substrate of the elastic energy density $\mathcal{E}^{el}(\boldsymbol{r},z)$

$$\mathcal{F}^{el} = \int_{z<h(\boldsymbol{r})} \mathcal{E}^{el}(\boldsymbol{r},z)d\boldsymbol{r}dz. \tag{4}$$

B. Anisotropic surface energy

The contribution μ^s of the surface energy $\mathcal{F}^s$ to the chemical potential μ follows merely from Eqs. (2) and (3) and reads

$$\mu^s = \gamma\kappa + \frac{\partial\gamma}{\partial h}\frac{1}{\sqrt{1+|\nabla h|^2}} - \frac{2}{\sqrt{1+|\nabla h|^2}}h_j h_{ij}\frac{\partial\gamma}{\partial h_i} - \sqrt{1+|\nabla h|^2}\left[h_{ij}\frac{\partial^2\gamma}{\partial h_i\,\partial h_j} + h_i\frac{\partial^2\gamma}{\partial h\,\partial h_i}\right], \tag{5}$$

with summation over repeated indices $i,j=x,y$ and where κ is the mean curvature

$$\kappa = -\frac{h_{ii}+\vartheta_{ij}h_{i^*}h_{j^*}h_{ij}}{(1+|\nabla h|^2)^{3/2}}, \tag{6}$$

with $\vartheta_{xx}=\vartheta_{yy}=-\vartheta_{xy}=-\vartheta_{yx}=1$ and with $x^*=y$ and $y^*=x$. As a first approximation, we examine a decomposition of the surface energy where wetting and anisotropy are disentangled such as

$$\gamma(h,\boldsymbol{n}) = \gamma_f[1+\gamma_{\boldsymbol{n}}(\boldsymbol{n})+\gamma_h(h)], \tag{7}$$

where $\gamma_f=\gamma(h\to\infty,\boldsymbol{n}=\hat{\boldsymbol{z}})$ is the surface energy of a thick film with a (001) surface. With this assumption, the cross derivatives present in the last term of Eq. (5) vanish. Wetting effects are characterized by the function γ_h, see, e.g., Refs. 23 and 56, which we choose, given *ab initio* calculations on Si/Ge systems[31,57] as

$$\gamma_h(h) = c_w \exp(-h/\delta_w), \tag{8}$$

where c_w and δ_w are the amplitude and the depth of the energy variation with the film height. For a Ge_xSi_{1-x} film, we fit atomistic results by setting $c_w=0.09$ for $x=0.25$ and δ_w given by the lattice parameter.

The anisotropic term is rewritten as $\gamma_{\boldsymbol{n}}(\boldsymbol{n})=\gamma^a(\boldsymbol{n})-\gamma^a(\hat{\boldsymbol{z}})$ where the anisotropic function γ^a describes different minima of the surface energy at preferential orientations $\boldsymbol{n}_\alpha$. Different parametrizations of minima in the gamma plot are available, see, e.g., Refs. 45, 49, and 58–61. We choose here to depict them as

$$\gamma^a(\boldsymbol{n}) = -\sum\nolimits_\alpha A_\alpha \exp[-\eta_\alpha\sqrt{1-(\boldsymbol{n}\cdot\boldsymbol{n}_\alpha)^2+\epsilon_\alpha}], \tag{9}$$

where A_α characterizes the depth of the minimum for $\boldsymbol{n}_\alpha$ and η_α, its extent over $\boldsymbol{n}$. If ϵ_α were zero, the argument of the exponential would reduce to $|\sin\Theta|$ where Θ is the angle between $\boldsymbol{n}$ and $\boldsymbol{n}_\alpha$, and would stand for the step creation energy[2] which introduces singularities when $\Theta=0$. We regularize this singularity with the parameter ϵ_α, see, e.g., Ref. 59, which beside technical benefit, can be linked to thermal rounding of the cusp of the facet orientation, see, e.g., Ref. 62.

As regards Si/Ge films deposited on a nominal (001) surface, one must regard minima corresponding to the (001) and (105) orientations. The (001) orientation is expected to be stable but not a facet. Indeed, the development of the elastic instability with a nucleationless scenario[17,18] can be rationalized with this nonfacet hypothesis.[45,63] Hence, we specify a shallow minimum of the surface energy near $h_x=h_y=0$. On the other hand, the appearance of square-base pyramids with the (105) facets in strained films[17,18,27] indicates that this orientation is another minimum for the surface energy. This minimum is in fact induced by strain,[30] yet we will not include at first order its dependence on the local strain and will consider that the mean strain induces a minimum for (105). As seen in scanning tunnel microscope images,[63] the (105) facets for pyramids as opposed to the roughness of the prepyramids near (001), indicate that the minima for (105) is stiffer than the one for (001). Hence, we will assign $\epsilon_0=10^{-1}$ and $\eta_0=10$ for $\boldsymbol{n}_0=(0,0,1)$ corresponding to the (001) orientation, and $\epsilon_1=10^{-3}$, $\eta_1=15$ for the four (105) minima, at $n_1,\ldots,n_4=(\pm\sin\theta_1,0,\cos\theta_1)$ and $(0,\pm\sin\theta_1,\cos\theta_1)$ where $\tan\theta_1=1/5$, see Figs. 2 and 3. As found by *ab initio* calculations,[30] one can expect this minimum to be on the order of 1% below the minimum at (001). We will take in the following $\gamma_{\boldsymbol{n}}(\boldsymbol{n}_\alpha)=-0.7\%$ for the (105) minima as compared to the (001) one. The dynamics found below is in fact not sensitive to this precise choice as long as it remains on the order of a few percent. Finally, the limit at large slope is taken as +2.6% larger than the value for (001),

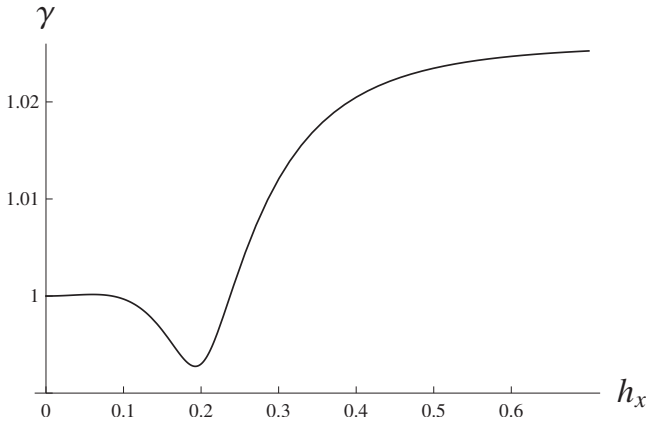

FIG. 2. Dependence of the surface energy (in units of γ_f) on the local slope $h_x=\tan\theta$ for $h_y=0$, where θ is the angle between the normal $\boldsymbol{n}$ and the z axis. The first shallow minimum at $h_x=0$ corresponds to the (001) orientation while the other minimum at $h_x=\tan\theta_1=1/5$ describes the (105) orientation. Other minima are present for $(h_x=-\tan\theta_1, h_y=0)$ and $(h_x=0, h_y=\pm\tan\theta_1)$.

with again little consequence on the physical properties. Other orientations, such as (113) and (15 3 23) could be also included as other minima and could be relevant for domes and hut islands[7,15] but we will restrict our study to thin enough films with only small pyramids with (105) facets.

C. Elastic contribution

The elastic contribution to the chemical potential, Eq. (2), is merely the elastic energy density at the free surface $\mu^{el}=\mathcal{E}^{el}[\boldsymbol{r}, z=h(\boldsymbol{r})]$, which is given by

$$\mu^{el}=\frac{1}{2}\sigma_{ij}e_{ij}[z=h(\boldsymbol{r})], \tag{10}$$

where $\boldsymbol{\sigma}$ and $\boldsymbol{e}$ stand for the stress and strain tensors. Mechanical equilibrium is supposed to be achieved on time scales much shorter than the diffusion and growth time scales so that the displacement $\boldsymbol{u}$ satisfies the Lamé equations

$$\partial_j\sigma_{ij}\equiv L(\boldsymbol{u})=0, \tag{11}$$

where $i,j=x,y,z$. We consider here linear isotropic elasticity, where

$$\sigma_{ij}=\frac{E}{1+\nu}\left[e_{ij}+\frac{\nu}{1-2\nu}e_{jj}\delta_{ij}\right] \tag{12}$$

with the Young modulus E and Poisson ratio ν. Elastic anisotropy could be included at that stage but we aim primarily at exhibiting the role of the dominant surface energy anisotropy and will therefore discard it. Moreover, in order to simplify calculations, the film and substrate elastic constants are supposed to be equal unlike the case treated in Ref. 41 where different elastic coefficients were considered. This hypothesis greatly simplifies the analysis as shown below. Small differences in the final result may arise when considering different elastic constants, as the comparison with Ref. 41 shows.

The film with a native lattice parameter a^f is coherently deposited on the substrate with lattice parameter a^s. Displacements are computed with respect to the substrate reference state in the x and y directions,

$$e_{ij}=\frac{1}{2}(\partial_j u_i+\partial_i u_j)-\bar{\delta}\delta_{ij}(\delta_{ix}+\delta_{jy})\theta(z) \tag{13}$$

with the misfit $\bar{\delta}=(1-a_f/a_s)$ and $\theta(z)$, the Heaviside function equal to 1 for $z>0$ and 0 otherwize. The coherence between the film and substrate enforces the continuity of displacements and stresses at the film/substrate interface, and implies

$$\boldsymbol{u}|_{z=0^-}=\boldsymbol{u}|_{z=0^+}, \tag{14}$$

$$\boldsymbol{\sigma}[\boldsymbol{u}]\cdot\mathbf{z}|_{z=0^-}=\boldsymbol{\sigma}[\boldsymbol{u}]\cdot\mathbf{z}|_{z=0^+}. \tag{15}$$

Finally, the free surface is supposed to be in contact with a vanishing vapor pressure and is characterized by a negligible surface stress,[40] so that the stress-free surface satisfies

$$\boldsymbol{\sigma}[\boldsymbol{u}]\cdot\mathbf{n}|_{z=h(\boldsymbol{r})}=\mathbf{0} \tag{16}$$

and we fix the origin of displacements with the condition $\boldsymbol{u}|_{z=-\infty}=\mathbf{0}$.

The Lamé equations can be conveniently handled using Fourier transforms with respect to $\boldsymbol{r}$,

$$\mathcal{F}[h](\boldsymbol{k})\equiv\hat{h}(\boldsymbol{k})=\frac{1}{(2\pi)^2}\int d\boldsymbol{r}e^{i\boldsymbol{k}\cdot\boldsymbol{r}}h(\boldsymbol{r}). \tag{17}$$

The solution of Eq. (11) can then be written as

$$\boldsymbol{u}=\boldsymbol{u}_0+\boldsymbol{u}_1, \tag{18}$$

with the flat film solution

$$\boldsymbol{u}_0=[0,0,\alpha z\theta(z)], \tag{19}$$

where $\alpha=2\bar{\delta}\nu/(1-\nu)$ and with

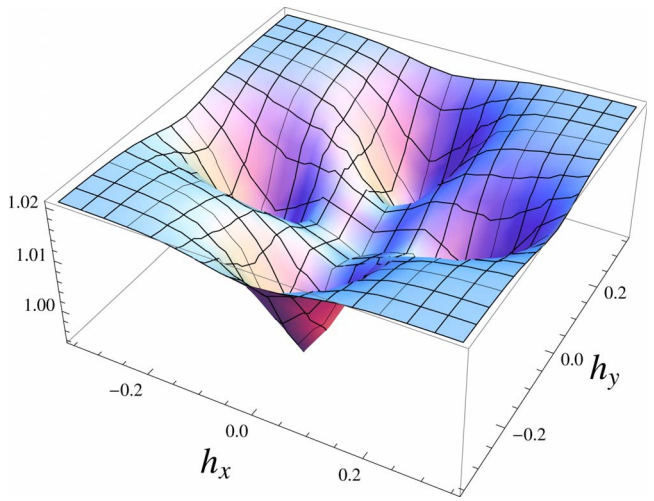

FIG. 3. (Color online) Dependence of the surface energy (in units of γ_f) on the local slopes h_x and h_y with one minimum for the (001) orientation and four minima corresponding to the (105) orientation.

$$\hat{\boldsymbol{u}}_1(\boldsymbol{k},z)=\frac{1}{3-4\nu}e^{|\boldsymbol{k}|z}\begin{pmatrix}\frac{1}{|\boldsymbol{k}|}\{C_x[k_x^2z+(3-4\nu)|\boldsymbol{k}|]+C_yk_xk_yz+C_z|\boldsymbol{k}|\mathrm{i}k_xz\}\\ \frac{1}{|\boldsymbol{k}|}\{C_xk_xk_yz+C_y[k_y^2z+(3-4\nu)|\boldsymbol{k}|]+C_z|\boldsymbol{k}|\mathrm{i}k_yz\}\\ z(\mathrm{i}k_xC_x+\mathrm{i}k_yC_y)-C_z(|\boldsymbol{k}|z+3-4\nu)\end{pmatrix},\tag{20}$$

where the three constants C_i are to be determined given the boundary conditions [Eq. (16)]. The general solution for $\boldsymbol{u}$ should *a priori* involve both $e^{|\boldsymbol{k}|z}$ and $e^{-|\boldsymbol{k}|z}$ contributions in the film and the substrate. The $e^{-|\boldsymbol{k}|z}$ terms trivially vanish in the substrate but they also vanish in the film as shown in Appendix A. Hence, the solution for $\boldsymbol{u}_1$ involves only three constants instead of the *a priori* six constants involved in the second-order three-dimensional Lamé equations.

To solve the surface free boundary condition, we use the small-slope approximation where the surface slopes are supposed smaller than unity so that one can decompose $h(\boldsymbol{r})$ according to

$$h(\boldsymbol{r})=h_0+\epsilon h_1(\boldsymbol{r}),\tag{21}$$

where h_0 is the mean film height and ϵ, a small parameter. The boundary condition [Eq. (16)] can then be solved using expansions in power series of ϵ

$$C_i=\sum_{n=1}^{\infty}\epsilon^nC_i^{(n)},\tag{22}$$

where the sum starts with $n=1$ as $\boldsymbol{u}_0$ is already the solution for a plane film. Finally, one finds

$$\begin{bmatrix}C_x^{(1)}\\ C_y^{(1)}\\ C_z^{(1)}\end{bmatrix}=\bar{\delta}\frac{(1+\nu)}{(1-\nu)}\frac{e^{-|\boldsymbol{k}|h_0}}{|\boldsymbol{k}|}\begin{bmatrix}[2(1-\nu)-|\boldsymbol{k}|h_0]\mathrm{i}k_x\hat{h}_1\\ [2(1-\nu)-|\boldsymbol{k}|h_0]\mathrm{i}k_y\hat{h}_1\\ (1-2\nu+|\boldsymbol{k}|h_0)|\boldsymbol{k}|\hat{h}_1\end{bmatrix}\tag{23}$$

at first order while the second order is given by convolutions

$$C_i^{(2)}=\bar{\delta}\frac{(1+\nu)}{(1-\nu)}\int d\boldsymbol{k}_1\frac{e^{-|\boldsymbol{k}|h_0}}{|\boldsymbol{k}_1||\boldsymbol{k}^2}\hat{h}_1(\boldsymbol{k}_1)\hat{h}_1(\boldsymbol{k}-\boldsymbol{k}_1)D_i(\boldsymbol{k},\boldsymbol{k}_1),\tag{24}$$

where

$$\begin{aligned}D_x(\boldsymbol{k},\boldsymbol{k}_1)=&\,\mathrm{i}k_x|\boldsymbol{k}_1|(1-2\nu-|\boldsymbol{k}|h_0)\boldsymbol{k}\cdot\boldsymbol{k}_1\\&+\frac{1}{|\boldsymbol{k}|}\{-4(1-\nu)[\mathrm{i}k_{1x}\boldsymbol{k}^2\boldsymbol{k}\cdot\boldsymbol{k}_1+\mathrm{i}k_x\nu(\boldsymbol{k}\wedge\boldsymbol{k}_1)^2]\\&+2|\boldsymbol{k}|\mathrm{i}k_xh_0[(\boldsymbol{k}\cdot\boldsymbol{k}_1)^2+\nu(\boldsymbol{k}\wedge\boldsymbol{k}_1)^2]\}\end{aligned}\tag{25}$$

with a symmetric relation for D_y where x and y are exchanged while the last constant is given by

$$\begin{aligned}D_z(\boldsymbol{k},\boldsymbol{k}_1)=&[2(1-\nu)+h_0|\boldsymbol{k}|]|\boldsymbol{k}||\boldsymbol{k}_1|\boldsymbol{k}\cdot\boldsymbol{k}_1\\&-2\{(1-2\nu+|\boldsymbol{k}|h_0)[(\boldsymbol{k}\cdot\boldsymbol{k}_1)^2+\nu(\boldsymbol{k}\wedge\boldsymbol{k}_1)^2]\}.\end{aligned}\tag{26}$$

The full form of the solution for the displacement $\boldsymbol{u}$ is displayed in Appendix B. From this solution, we compute the elastic chemical potential [Eq. (10)] which reads

$$\begin{aligned}\mu^{el}/\mathcal{E}_0=&\,1-\omega\mathcal{H}_{ii}(h)+\omega(2h\boldsymbol{\Delta}h+|\boldsymbol{\nabla}h|^2)\\&+\omega[2\mathcal{H}_{ij}[h\theta_{ijkl}\mathcal{H}_{kl}(h)]+\mathcal{H}_{ij}(h)\theta_{ijkl}\mathcal{H}_{kl}(h)],\end{aligned}\tag{27}$$

where $\omega=2(1+\nu)$, $\mathcal{E}_0=E\bar{\delta}^2/(1-\nu)$ is the elastic energy density of a flat film while the nonlocal operator $\mathcal{H}$, linked to the long-range elastic interactions, is given by

$$\mathcal{H}_{ij}[h]=\mathcal{F}^{-1}[(k_ik_j/|\boldsymbol{k}|)\hat{h}(\boldsymbol{k})].\tag{28}$$

The dimension index θ_{ijkl} is $\theta_{ijij}=1$ for any $i,j=x,y$ whereas $\theta_{iijj}=-\theta_{ijji}=\nu$ for $i\neq j$ while it vanishes otherwise. Note that the chemical potential [Eq. (27)] has to be invariant under the transformation $h_0\rightarrow h_0+\delta h_0$. Indeed, the flat film solution $\boldsymbol{u}_0$, cf. Eq. (18), is independent of the arbitrary free surface level beside the trivial localization of the film while the shape induced displacement $\boldsymbol{u}_1$, equal to the solution for a single film subject to a biaxial stress, is also independent of the reference for film heights. In the solution for the elastic chemical potential [Eq. (27)], the term $h\boldsymbol{\Delta}h$ seems to violate this invariance but the latter is restored when this term is combined with $\mathcal{H}_{ij}[h\mathcal{H}_{kl}[h]]$. As $\mathcal{H}_{ij}[h]$ is also invariant under the Galilean transformation, the solution (27) as a whole satisfies this property. Finally, we also find the total elastic energy [Eq. (4)], which follows directly from integration of the elastic energy density and reads at first orders

$$\mathcal{F}^{el}/\mathcal{E}_0=\int d\boldsymbol{r}\{h(\boldsymbol{r})-(1+\nu)\epsilon h_1(\boldsymbol{r})\mathcal{H}_{ii}[\epsilon h_1(\boldsymbol{r})]\}.\tag{29}$$

D. Evolution equation

Given the solution for the surface and elastic chemical potential [Eqs. (5) and (27)], the evolution equation follows merely from mass conservation [Eq. (1)]. We consider the space scale

$$l_0 = \gamma_f/[2(1+\nu)\mathcal{E}_0] \tag{30}$$

resulting from the competition between the typical surface energy γ_f and the elastic energy $\mathcal{E}_0$, which can be associated with the time scale

$$t_0 = l_0^4/(D\gamma_f) \tag{31}$$

with diffusion coefficient D. Eventually, in units of l_0 and t_0, the evolution equation reads up to second order

$$\begin{aligned}\frac{\partial h}{\partial t} = F + \mathbf{\Delta}\Bigg\{ & -[1+\gamma_{\boldsymbol{n}}(\boldsymbol{n})+\gamma_h(h)]\mathbf{\Delta}h + \left[1-\frac{1}{2}|\boldsymbol{\nabla}h|^2\right]\frac{d\gamma_h}{dh} \\ & - h_{xx}\frac{\partial^2\gamma_{\boldsymbol{n}}}{\partial h_x^2} - 2h_{xy}\frac{\partial^2\gamma_{\boldsymbol{n}}}{\partial h_x\,\partial h_y} - h_{yy}\frac{\partial^2\gamma_{\boldsymbol{n}}}{\partial h_y^2} \\ & - 2(h_x h_{xx}+h_y h_{xy})\frac{\partial\gamma_{\boldsymbol{n}}}{\partial h_x} - 2(h_x h_{xy}+h_y h_{yy})\frac{\partial\gamma_{\boldsymbol{n}}}{\partial h_y} - \mathcal{H}_{xx}(h) \\ & - \mathcal{H}_{yy}(h) + 2h\mathbf{\Delta}h + |\boldsymbol{\nabla}h|^2 + 2\mathcal{H}_{xx}[h(\mathcal{H}_{xx}[h]+\nu\mathcal{H}_{yy}[h])] \\ & + 4(1-\nu)\mathcal{H}_{xy}[h\mathcal{H}_{xy}[h]] + 2\mathcal{H}_{yy}[h(\mathcal{H}_{yy}[h]+\nu\mathcal{H}_{xx}[h])] \\ & + \mathcal{H}_{xx}[h]^2 + \mathcal{H}_{yy}[h]^2 + 2(1-\nu)\mathcal{H}_{xy}[h]^2 \\ & + 2\nu\mathcal{H}_{xx}[h]\mathcal{H}_{yy}[h]\Bigg\}. \end{aligned} \tag{32}$$

This equation is parameterized by the dimensionless deposition flux F in units of t_0 and by the parameters of the wetting potential γ_h and of the anisotropy $\gamma_{\boldsymbol{n}}$.

III. NUMERICAL RESULTS

The evolution equation displayed in Eq. (32) was solved numerically using a pseudospectral algorithm in a $L\times L$ system with length $L=128$ using N^2 modes with $N=256$. For the numerical implementation we used a pseudospectral method using a fourth-order time stepping exposed in details in Ref. 64. We choose to depict a $Ge_{0.25}Si_{0.75}$ film deposited on a Si substrate, with the lattice parameters $a_s=0.27$ nm and $a_f=1.01a_s$, with the elastic parameters $\nu^f=0.28$ and $E^f=1.2310^{11}$ kg m^{-1} s^{-2} and with a surface energy $\gamma_f=1.3$ J/m^2. The diffusion coefficient is associated with a typical Arrhenius law $D=D_s\exp[-E_d/k_BT]a_f^4/k_BT$ with $E_d=0.83$ eV, and $D_s=8.4510^{-10}$ m^2/s, see, e.g., Ref. 55. The growth temperature is 700 °C. The intrinsic deposition noise, together with the natural roughness of the SiGe interfaces, are replaced here by a noisy initial condition which corresponds to a roughness of amplitude 1 monolayer (ML).

A. First stages

Our goal is to study the long-time dynamics of strained films evolving via surface diffusion. In order to be closer to the experimental procedure, we first grow h_{fin} monolayers until a finite time at which the growth flux is interrupted and annealing begins, see Fig. 4. The simulations are thence parametrized by the height of the deposited film h_{fin} which characterizes the volume of matter at the end of deposition before annealing begins. Hence, for a projected surface L^2, the volume of matter in the film at the end of deposition is

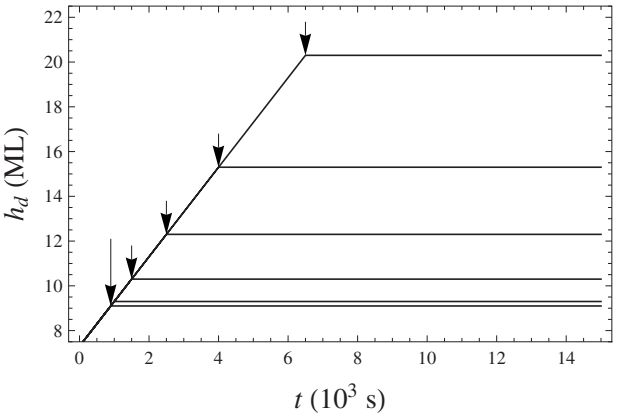

FIG. 4. Sketch of the numerical procedure for growth and deposition. The deposited height h_{dep} characterizing the amount deposited at time t for different values of the final deposited height h_{fin}. The six values $h_{fin}=(9.0,9.2,10.2,12.2,15.2,20.2)$ ML are labeled as (a,b,c,d,e,f) from bottom to top. The arrows mark the deposition flux interruption time where the deposition flux is turned off and where annealing begins. A double-longer arrow is shown for visual clarity for the two slightly different values of h_{fin} in the two first a and b cases.

$V=L^2h_{fin}$. We vary h_{fin} between a value close to the instability threshold (below which no instability occurs as defined in the following) to a value less than the transition to large islands (see below), the study of which being beyond the scope of the present analysis. For the sake of clarity, we mark with arrows in our numerical results the different times at which the deposition flux is stopped for the different simulations with different h_{fin}. The flux was chosen neither too low so that different evolutions occur, nor too strong so that some evolution may happen during growth and we therefore scanned different growth modes by varying h_{fin}.

The growth rate of a perturbation $h_1(\boldsymbol{r})=e^{i\boldsymbol{k}\cdot\boldsymbol{r}+\sigma t}$ with a wave vector $\boldsymbol{k}$ behaves typically as[41] $\sigma(\boldsymbol{k},h_0)\propto -c(h_0)\boldsymbol{k}^2+|\boldsymbol{k}|^3-\boldsymbol{k}^4$, where c depends on the mean film height h_0. For h_0 below the instability threshold $h_c\simeq 8$ ML,[65] σ is always negative for all $\boldsymbol{k}$ and the evolution leads to a flat stable film. We are interested by the regime above h_c where σ displays a maximum with a positive value. The instability leads first to a surface characterized by the wavelength corresponding to the maximum of $\sigma(\boldsymbol{k})$ and the evolution of h_1 governed by the linear contributions is mainly exponential in time. This stage is promptly followed by coarsening with well-defined islands surrounded by a wetting layer, where nonlinear and wetting effects fully come into play.[41] During this stage, large islands grow at the expense of smaller ones due to mass transfer via the wetting layer similarly to isotropic systems.[41] These prepyramidal islands grow with an increasing aspect ratio and thence with increasing slopes until they reach the slopes corresponding to the (105) facets, see Fig. 5. After this stage, square- or pyramid-base pyramids arise and evolve with a constant aspect ratio. Ultimately, the film reaches a stationary regime where the roughness w, island density ρ and coverage θ (defined by the projected area of the islands above the wetting layer) remain constant, see Figs. 6–8, as discussed in Sec. III B.

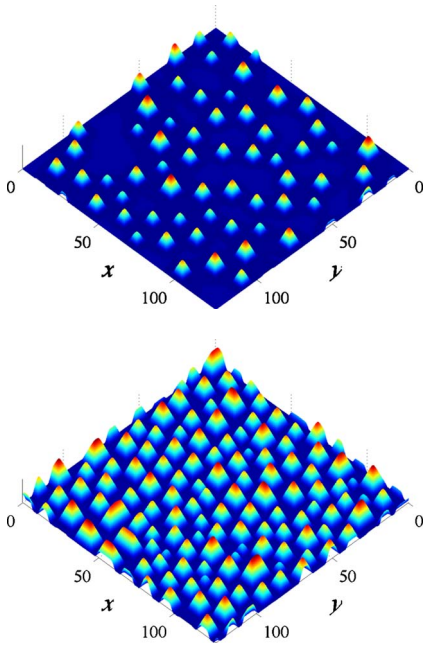

FIG. 5. (Color online) Stationary regime of the numerical simulations of Eq. (32). The box of size is $L=128l_0$ with $l_0=27$ nm while the total amount of matter is $h_{fin}=9.0$ ML (top) and 20.2 ML (bottom). The anneal time is 300 min (top) and 250 min (bottom). The movie of the time evolution is available online (Ref. 66).

We have chosen six different values for $h_{fin}=(9.0,9.2,10.2,12.2,15.2,20.2)$ ML labeled (a,b,c,d,e,f). These values are chosen above h_c but not too large in order to avoid the appearance of large isotropic islands which relax more efficiently the stress but would, in connection with Si/Ge films, require additional preferential directions, see, e.g., Ref. 45. For the (a,b,c,d) cases, the roughness, surface coverage and island density barely increase before annealing so that most of the dynamical evolution takes place during annealing. These doglegged curves display inflection points which are shifted to the left when h_{fin} increases, indicating that the evolution occurs sooner for thicker films as a result of the dependence of the growth rate $\sigma(\boldsymbol{k})$ on h_0 which is characterized by larger positive regions

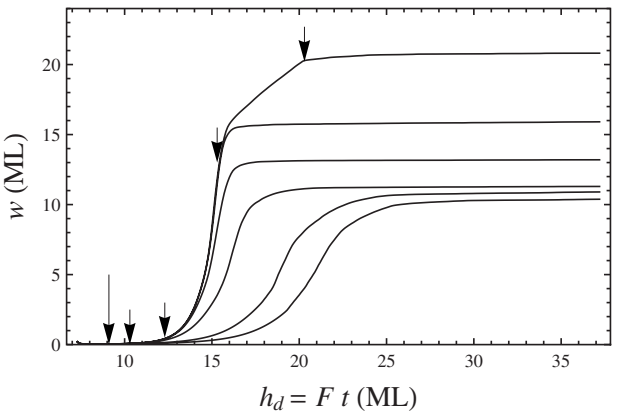

FIG. 6. Numerical simulations of Eq. (32). Evolution of the surface roughness versus time for, from bottom to top, the six cases (a,b,c,d,e,f).

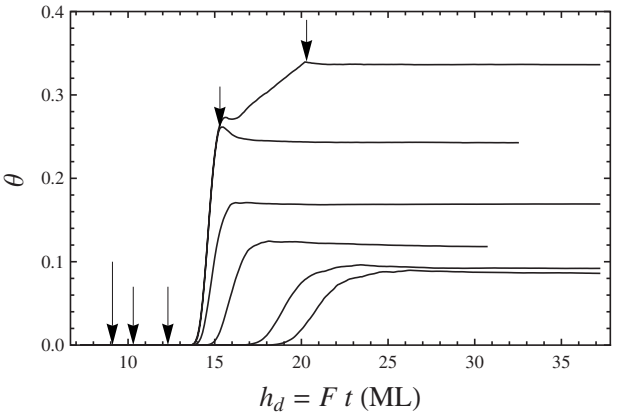

FIG. 7. Numerical simulations of Eq. (32). Evolution of the surface coverage versus time for, from bottom to top, the cases (a,b,c,d,e,f).

in $\boldsymbol{k}$ as h_0 increases. The latter dependence is a consequence of the wetting potential.[41] On the other hand, in the cases (e) and (f), the islands (which already entered their nonlinear stage) arise during growth. This is notably visible for the case (f) in the roughness and coverage plots in Figs. 6 and 7. After the initial exponential increase, the roughness and coverage time evolution is linear when fully facetted pyramids are present. These islands evolve in a self-similar manner as their aspect ratio is kept fixed by the preferential orientations and their height increases linearly with time during growth due to mass conservation. Consequently, their coverage and roughness increase merely linearly while their density is roughly constant, see Fig. 8. However, a careful study of Figs. 7 and 8 reveals that the island density and (less pronouced) island coverage slightly decrease after reaching their maximal value, as some coarsening occurs where small isotropic prepyramids disappear to the benefit of large pyramids. Finally, we note that the morphology of the growing islands is also modified by the amount of matter. For low h_{fin}, the pyramids are always square base while for higher h_{fin}, i.e., in the cases (e) and (f), the islands adopt mainly a square-base shape but some of them are rectangular pyramids, see Fig. 9. This observation can be rationalized by the

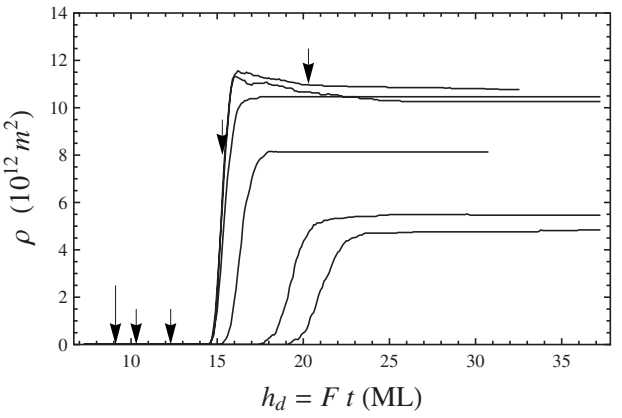

FIG. 8. Numerical results of Eq. (32). Evolution of the island density versus time for, from bottom to top, the cases (a,b,c,d,e,f).

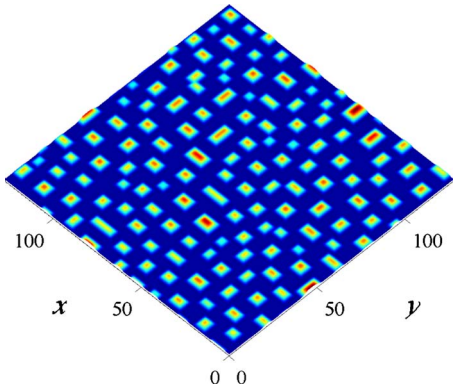

FIG. 9. (Color online) Stationary regime of the numerical simulation of Eq. (32) for $h_{fin}=15.2$ ML and anneal time of 500 min.

elastic energetic calculations by Tersoff and Tromp,[67] which shows that small islands adopt a compact symmetric shape while larger ones minimize their energy with an elongated shape.

B. Interrupted coarsening

In all the cases under investigation, island coarsening stops after some time during annealing and the surface properties display plateaux, see Figs. 6–8. The surface is then characterized by an assembly of square- or (less frequent) rectangular-base pyramids, see Fig. 5. Contrarily to the isotropic case,[40,41] the coarsening is interrupted due to the additional ingredient of the surface energy anisotropy. The anisotropy amplitude is a natural parameter for the interrupted coarsening to happen, and we checked by lowering the magnitude of the variation in γ_n that isotropic islands continuously coarsen when anisotropy is too low. This is the case for example when γ_n is −0.3% lower than its value for the (001) direction which is −0.7% lower than the value for large slopes. Eventhough, a small anisotropy as the one considered in Sec. II B is sufficient to originate a complete change in Ostwald ripening.

This scenario is in accord with the experimental findings by Berbezier *et al.*[29] showing that a 18 h anneal of Si/Ge islands grown after the elastic instability leads to an assembly of pyramidal islands which do not evolve. The comparison is also interesting as regards the surface morphology. The simulations together with the experiments reveal an assembly of islands with a noticeable size inhomogeneity and spatial disorder, see Fig. 10 eventhough the first stages of the instability were rather regular. This interrupted coarsening is intrinsically kinetic as we checked that for a given quantity of matter, starting with a noisy flat film or with a pyramidal shape drives the film in the first case to an assembly of dense islands and in the second case to a single island with a large exclusion zone.

The resolution of the elastic problem available through Eq. (32), allows to perform large-scale simulations of the surface properties and compute the statistical properties of the islands resulting from the interrupted coarsening. An experimentally relevant parameter that we can vary here is the total amount of matter given by h_{fin}. As shown in Fig. 11,

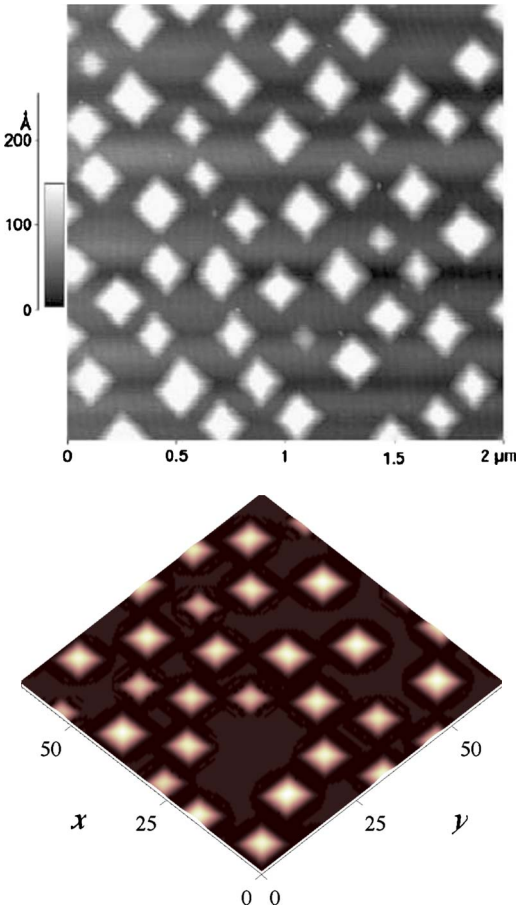

FIG. 10. (Color online) (top) Courtesy of Berbezier (Ref. 29). AFM image. 18 h anneal of a $Si_{0.75}Ge_{0.25}$ 50 Å thick film during an annealing at 550 °C. The [110] direction is horizontal. (bottom) Stationary regime resulting from the numerical simulations after annealing during 30 min.

the island density first increases strongly when $h_{fin}>h_c\simeq 8$ ML and then saturates (and slightly diminishes) after $h_{fin}\simeq 12$ ML. It is worth noting that the saturation occurs concomitantly with the introduction of rectangular-base pyramids supported by energetic considerations.[67] This saturation is not due to steric effects as it happens for a density lower than the upper bound resulting from steric arguments. Indeed, when one considers square-base pyramids with a base B and mean distance d, writing $B<d$ and assuming that all matter is collected by islands, leads to the upper bound $h_{fin}<d/30$ which is 30 ML given the typical mean distance $d\simeq 10$ in units of l_0 as revealed by the simulations. On the other hand, as shown on Fig. 12, the island mean volume is a nonmonotonous function of the quantity of matter, as it first decreases with h_{fin} before rising. The first decrease can be understood if one considers the initial stronger than linear increase in the island density with h_{fin}, see Fig. 11, in conjunction with mass conservation which relates linearly the total amount of matter with h_{fin}. The following increase is merely linear and is related to the density saturation while h_{fin} increases. Hence, varying solely the quantity of matter results in a change in both the mean island volume or island density in a coupled evolution.

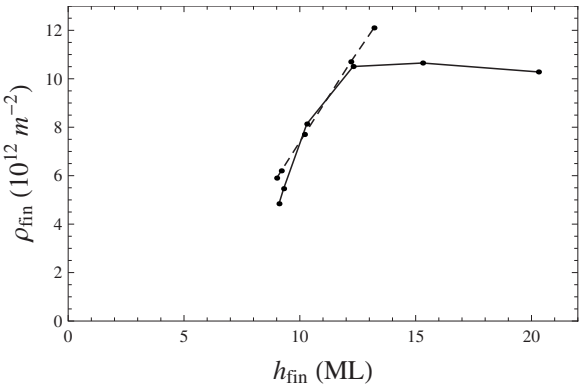

FIG. 11. Pyramide density (solid line) in the stationary state as function of the total amount of matter characterized by the final deposited mean film height h_{fin}. The dashed line results from the energetic pathway model discussed in Sec. IV with a fixed wetting layer $h=5.1$ ML.

Finally, we also characterize the island size distribution which is a crucial characteristic in the self-organization of crystal growth. The typical plots of these distributions for the cases (a), (e), and (f) are displayed in Fig. 13, after averaging over four simulations. Surprisingly, these distributions depend nonmonotonically on the amount of matter. The island size distribution is rather wide for low and high h_{fin}, while it is more peaked for intermediate values. We quantify the island size dispersion with the standard deviation Δv of these distributions. It is depicted in Fig. 14 and do reveal a minimum for $h_{fin} \simeq 12$ ML [case (d)]. Hence, the intrinsic dispersion of the island sizes, even though unavoidable, may be optimized by choosing a particular value of h_{fin}.

IV. PATHWAY MODEL

To obtain insight in the origin of the observed interrupted coarsening, we examine an energetic model in the spirit of Ref. 43 that we extend to describe energetic pathways. We first recall the basic ingredients of a monodisperse island model and then extend it to encompass island mutual transformation.

A. Uniform model

Let us first consider a uniform array of pyramids with volume V, width L, and fixed aspect ratio characterized by the angle α enforced by the film anisotropy, see Fig. 15. Each island occupies a capture zone of surface $1/n$ and lies on a wetting layer of height h. The system corresponds via mass conservation to a flat film (referred to as the reference system) of height h_0 given by

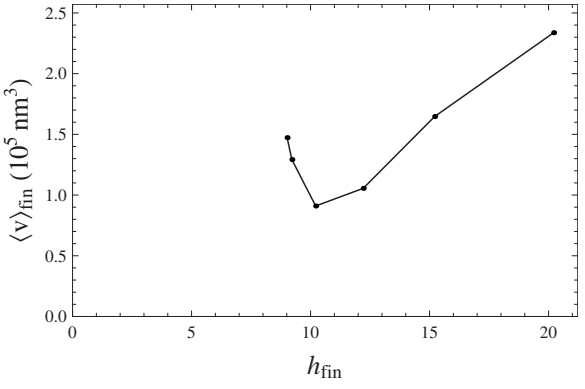

FIG. 12. Mean island volume $\langle v \rangle$ in the stationary state as function of the amount of matter.

$$h = h_0 - nV. \tag{33}$$

The energy difference ΔE between the island array and the reference state is given per unit cell by[43]

$$\Delta E = \gamma_f L^2/\cos\,\alpha - L^2\gamma(h_0) + (1/n - L^2)[\gamma(h) - \gamma(h_0)] - \lambda_e V. \tag{34}$$

The first term stands for the cost in surface energy of the islands where γ_f is the facet surface energy of the islands. The second and third terms are associated with wetting which manifests itself through the h dependence of the flat film surface energy that we characterize similarly to Eq. (8),

$$\gamma(h) = \gamma_w[1 + c_w \exp(-h/\delta_w)]. \tag{35}$$

(We checked that a wetting dependence of the facet surface energy would not change the results given below.) Finally, the last term stands for the elastic energy difference. The latter is given by Eq. (29) where one can check that for pyramids with a given aspect ratio, $\mathcal{F}^{el}$ is proportional to the volume defined above the pyramid base. This property follows merely when one looks at two similar pyramids linked by the relation $h_2(\boldsymbol{r}) = \eta h_1(\eta^{-1}\boldsymbol{r})$, where h_i is the film height with respect to the pyramid base, and then realizes that both $\mathcal{F}^{el}$ and the volume scale as η^3. Computing numerically $\mathcal{F}^{el}$ given by Eq. (29) for a pyramidal shape using discrete Fourier transforms, we find $\lambda_e = \mathcal{E}_0(1+\nu)p$ with $p=0.193$.

The energy difference [Eq. (34)] can be rewritten as

$$\Delta E(v,n,h_0)/E_s = \tilde{\gamma}(h_0)v^{2/3} + [v_0^{2/3}(n) - v^{2/3}](e^v - 1) - \tilde{\lambda}_e(n)v \tag{36}$$

with the dimensionless volume

$$v = nV/\delta_w \tag{37}$$

and the parameters

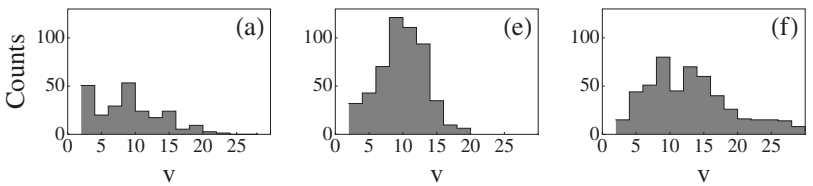

FIG. 13. Island volume distributions from the numerical simulations for the cases (a), (e), and (f), where v is given in units of l_0.

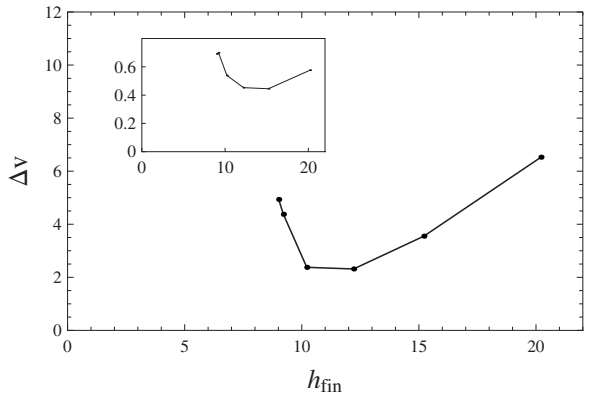

FIG. 14. Standard deviation Δv of the island size distribution as function of the amount of matter and (inset) relative width $\Delta v/\langle v\rangle$.

$$\tilde{\gamma}(h_0) = [\gamma_f/\cos\,\alpha - \gamma(h_0)]/\gamma_w c_w e^{-h_0/\delta_w}, \tag{38}$$

$$\tilde{\lambda}_e(n) = \delta_w \lambda_e / n E_s, \tag{39}$$

$$v_0(n) = \tan\,\alpha/6n^{1/2}\delta_w, \tag{40}$$

and $E_s = \gamma_w c_w e^{-h_0/\delta_w}(6\delta_w/n\,\tan\,\alpha)^{2/3}$. We consider in the following the parameters used in the simulations of Sec. III where γ_f is given by $1+\gamma_n$, cf. Eq. (7), at the minimum for the (105) orientation characterized by $\tan\,\alpha = 1/5$. Simulations reveal stationary states with a typical density of order $n \simeq 10^{-6} a_f^{-2}$. Moreover, mass conservation [Eq. (33)] enforces the bound $v < h_0/\delta_w$.

As shown in Ref. 43, the typical variation in ΔE as function of the uniform island volume V for a fixed island density and a given amount of matter h_0, displays a minimum for a characteristic volume V_c. The latter results from the competition between the elastic energy which decreases as $-\lambda_e V$ for islands with a fixed aspect ratio (given by the surface energy anisotropy) and the wetting energy characterizing peeling of the film for low wetting-layer heights which correspond, see Eq. (33), to large volumes V. A typical plot of this variation is shown in Fig. 16 where the first local maxima is due to the initial surface energy barrier. However, as discussed in Ref. 43, the minimum ΔE_c decreases monotonously by decreasing the island density n so that a noninterrupted coarsening is expected. Hence, this description cannot shed light on the interrupted coarsening observed in experiments and simulations.

B. Two islands model

The pathway for the island coarsening in the previous model is associated with a uniform decrease in the density n. However, coarsening in both experiments and simulations is

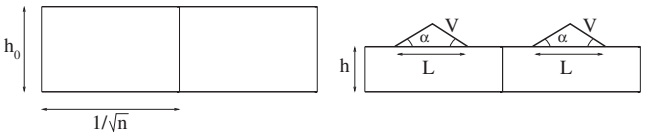

FIG. 15. Uniform island model

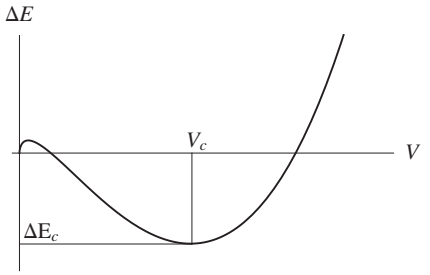

FIG. 16. Typical evolution of the energy difference [Eq. (36)] as function of the uniform island volume V.

first associated with a decrease in small islands for the benefit of bigger ones. In order to describe this evolution, we revisit the previous model by looking at two islands that can transfer matter to one another by surface diffusion. They are characterized by two volumes V_1 and V_2 above a wetting layer of height h, a capture zone of size $1/n$, and a fixed inclination α, see Fig. 17. Mass conservation now enforces the condition

$$h = h_0 - \frac{1}{2}\delta_w(v_1 + v_2), \tag{41}$$

where v_i is defined in Eq. (37). Neglecting elastic interactions between islands, the total energy is

$$\Delta E_{tot}(v_1, v_2) = \Delta E(v_1) + \Delta E(v_2). \tag{42}$$

Choosing the parameters that were used in the simulations and a typical density $n \simeq 10^{-6} a_s^{-2}$ as an order of magnitude, we plot in Fig. 18 the energy per atom as function of V_1 and V_2 for a given amount of matter $h_0 = 10$ ML. This energetic pathways indicates that the system can exhibit a valley of states with similar energy. This valley is roughly located along the dashed line defined as $V_1 + V_2 = 2V_c$, where V_c is the characteristic volume of the uniform model at the same density as defined in A. The point in the middle at $V_1 = V_2 = V_c$ is in fact a saddle point with a curvature in the valley direction (along $V_1 = 2V_c - V_2$) much larger than the curvature in the other principal direction (along $V_1 = V_2$). Quantitatively, the energy difference along the valley is negligible as the energy varies only about 10^{-5} eV between its extreme values. The latter variation being the driving force for coarsening, this energetic landscape can be interpreted as leading to a kinetically interrupted coarsening. The islands can be glued in a configuration where the energy variation during coarsening is negligible. This construction exhibits a characteristic volume V_c which, for $h_0 = 10$ ML and $n = 10^{-6} a_s^{-2}$, leads to $L_c \simeq 6 l_0$ which is the correct order of magnitude of the islands produced by the interrupted coarsening in simulations.

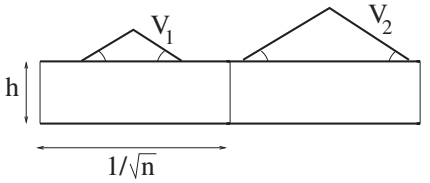

FIG. 17. Two islands exchanging mass via surface diffusion.

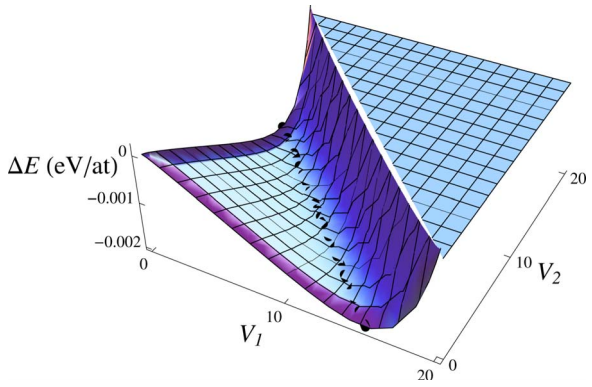

FIG. 18. (Color online) Energetic pathway for the coarsening of two shape-fix pyramids of volume V_1 and V_2. The energy is given in electron volt per atom. The dashed line indicates volume such as $V_1+V_2=2V_c$, where V_c is the critical volume defined in Sec. IV A. Volumes should satisfy the mass conservation constraint $v_1+v_2<2h_0/\delta_w$. The density is $n=10^{-6}a_f^{-2}$, as typical in simulations and the total amount of matter, $h_0=10$ ML.

Note that, if one would not allow for variations in the wetting-layer height, one would not get such a flat valley in the energy landscape. Hence the interrupted coarsening is allowed by possible (small) wetting-layer height variations.[68]

However, for a given h_0, the previous description does not allow for a determination of the mean island density. We try to give such an estimate by considering that the system is glued at the characteristic volume V_c as seen in Fig. 18. The condition $\partial E(v,n,h_0)/\partial V=0$ imposes an implicit relation among (v,n,h_0). A free fitting parameter is still left and we impose an extra constraint by fixing the wetting-layer height. Indeed, the different simulations for the cases (a)–(f) are characterized by a wetting layer roughly constant around $h\simeq 5$ ML. By setting $h=5.1$ ML, we get the best estimate for the expected island density. The result for this approximation is compared to the simulation results in Fig. 11. The agreement is rather good for low amounts of matter while it is significantly altered for thicker films. For the latter case, elastic interactions intra and inter pyramids show up. Indeed, rectangular shaped islands start to appear precisely when the island density as function of h_{fin} saturates, in accordance with elasticity theory.[67] The latter shape transition is not accounted for in our model and thus discrepancies are expected in this regime. However, the good order of magnitude for thin films indicates that the scenario of a valley with low varying energy states is suitable for understanding the observed interrupted coarsening.

V. CONCLUSION

We have studied the long-time dynamics of a thin-film subject to the morphological elastic instability, known as the Asaro-Tiller-Grinfeld instability, in a regime where anisotropy becomes prominent. We derive a continuum description accounting for surface effects (wetting and surface energy anisotropy) and linear elasticity. We considered a basic anisotropy with minima in the surface energy as function of the orientation describing a facet orientation relevant when sufficiently steep islands had grown. The long-range elastic interactions are computed in the small-slope approximation where the film free boundary introduces nonlinear geometrical contributions that we calculate explicitly in three dimensions obtaining nonlinear nonlocal energies. We solved numerically the evolution equation describing surface currents due to chemical-potential gradients and chose parameters suited for silicon-germanium films. A rather small anisotropy originates a complete change in the coarsening dynamics. In isotropic systems, large islands grow at the expense of smaller ones during an Ostwald coarsening which driving force is the efficient elastic relaxation allowed by an increase in the aspect ratio. The latter coarsening allows energy minimization and explains the first stage of ripening of the ATG instability where mainly isotropic prepyramids grow with an increasing aspect ratio thence with increasing slopes. However, once the islands grew enough, anisotropy becomes important as islands adopt pyramidal shapes with orientations corresponding to the facet minima. We find in this regime that island coarsening is suppressed by anisotropy and the system is glued in a metastable state characterized by square- or rectangular-base pyramids in accordance with experiments. We characterize the statistical properties of the resulting pyramids using large-scale simulations. We show that the island density first increases as function of the total amount of matter when mainly square-base pyramids are present while it saturates when rectangular-base pyramids start to appear. After an initial small decrease, the mean island volume mainly increases with the amount of matter indicating a way of tuning the island characteristics with a simple parameter. Moreover, we find that the island size distribution is more peaked for an optimal quantity of matter. Hence, we note that by varying the total amount of matter, different islands can be obtained with different density and volume. Finally, in order to give an explanation for the experimentally and numerically observed interrupted coarsening, we generalize an energetic model including anisotropy, elasticity and wetting, in order to describe energetic pathways relevant for the modeling Ostwald ripening. The latter pathways exhibit valleys of states with energy difference, which is the driving force for coarsening, which is vanishingly small and consequently suitable for explaining the interrupted coarsening. The predicted island density using this energetic picture augmented with an extra condition on the wetting-layer height compares favorably with the numerical results. A more detailed comparison between experiments and theory regarding the islands statistical properties is under current progress.

We note that the transition from pyramids with (105) facets to domes with extra facets, such as (113) or (15 3 23), see e.g., Ref. 7, may be studied using the present framework by adding other facets associated with additional minima in the surface energy as done in Ref. 45. The presence of facets and surface anisotropy are ubiquitous in many crystalline films so that the tools presented here may also be generalized to other materials provided proper modifications. Finally, the consideration of alloying of Si/Ge which may lead to spatial composition inhomogeneities due to intermixing and segregation is under current scrutiny.

ACKNOWLEDGMENTS

We thank Thomas Auphan, Isabelle Berbezier, Jean-Marc Debierre, Laurent Raymond, and Alberto Verga, for fruitful discussions and assistance.

APPENDIX A: SINGLE FILM AND FILM/SUBSTRATE GEOMETRIES

In order to justify the absence of $e^{-|\boldsymbol{k}|z}$ terms in the film in the solution (20), we show the equivalence between the film and substrate geometry and a strained semi-infinite solid which is valid when the film and substrate display equal elastic constants.

We first turn to the film/substrate case. We rewrite the boundary condition [Eq. (15)] making explicit reference to the misfit as

$$\boldsymbol{\sigma}[\boldsymbol{u},\bar{\delta}=0]\cdot\mathbf{z}|_{z=0^-}=\boldsymbol{\sigma}[\boldsymbol{u},\bar{\delta}]\cdot\mathbf{z}|_{z=0^+}, \tag{A1}$$

where the $\bar{\delta}$ dependence of the stress tensor originates from the reference state, cf. Eqs. (12) and (13). The decomposition [Eq. (18)] introduces in fact an external stress which can be deducted according to

$$\boldsymbol{\sigma}[\boldsymbol{u}_0+\boldsymbol{u}_1,\bar{\delta}]\cdot z=\boldsymbol{\sigma}[\boldsymbol{u}_1,\bar{\delta}=0]\cdot z. \tag{A2}$$

Moreover, as

$$\boldsymbol{\sigma}[\boldsymbol{u},\bar{\delta}]\cdot z-\boldsymbol{\sigma}[\boldsymbol{u},\bar{\delta}=0]\cdot z=[0,0,2E\bar{\delta}\nu/(2\nu^2+\nu-1)], \tag{A3}$$

is constant in the film and in the substrate in the case of equal elastic properties, one can check that the continuity relation (A1) reduces to

$$\boldsymbol{\sigma}[\boldsymbol{u}_1,\bar{\delta}]\cdot z|_{z=0^-}=\boldsymbol{\sigma}[\boldsymbol{u}_1,\bar{\delta}]\cdot z|_{z=0^+}. \tag{A4}$$

One can then consider the semi-infinite configuration made of a solid subject to a global biaxial stress in the x and y directions (referred to with superscripts *) and with the same free surface. In the latter geometry, we decompose displacements according to

$$\boldsymbol{u}^*=\boldsymbol{u}_0^*+\boldsymbol{u}_1^*, \tag{A5}$$

where

$$\boldsymbol{u}_0^*=(0,0,\alpha z). \tag{A6}$$

As shown in the following, $\boldsymbol{u}_1$ and $\boldsymbol{u}_1^*$ coincide. Indeed, one can first realize that $\boldsymbol{u}_1$ and $\boldsymbol{u}_1^*$ satisfy the same equation $L(\boldsymbol{u}_1)=\mathbf{0}$ (independently of $\bar{\delta}$), with the same boundary condition

$$\boldsymbol{\sigma}[\boldsymbol{u}_0+\boldsymbol{u}_1,\bar{\delta}]|_{z=h(\boldsymbol{r})}=\mathbf{0}. \tag{A7}$$

The displacement continuity at the film/substrate interface [Eq. (14)] and the stress continuity [Eq. (15)] which reduces to Eq. (A4) are automatically satisfied by $\boldsymbol{u}_1^*$ for which no discontinuity can happen for the arbitrary level $z=0$. Note that the hypothesis of equal film and substrate elastic constants turns out to be crucial at that stage as it allows the continuity relation (A4) to be the same in the film/substrate and single film configurations. Satisfying the same differential equation together with the same boundary conditions, the displacements $\boldsymbol{u}_1$ and $\boldsymbol{u}_1^*$ coincide due to the uniqueness of the solution.

APPENDIX B: SOLUTION FOR THE DISPLACEMENTS

Equations (20) and (22)–(26) define the solution for the displacement $\boldsymbol{u}$ which can be expanded as

$$\boldsymbol{u}_1=\sum_{n=1}^{\infty}\epsilon^n\boldsymbol{u}_1^{(n)}. \tag{B1}$$

The solution at first order reads

$$\boldsymbol{u}_1^{(1)}=\bar{\delta}\frac{1+\nu}{1-\nu}\frac{e^{|\boldsymbol{k}|(z-h_0)}}{|\boldsymbol{k}|}\begin{pmatrix}[2(1-\nu)+|\boldsymbol{k}|(z-h_0)]\mathrm{i}k_x\hat{h}_1\\ [2(1-\nu)+|\boldsymbol{k}|(z-h_0)]\mathrm{i}k_y\hat{h}_1\\ [1-2\nu-|\boldsymbol{k}|(z-h_0)]|\boldsymbol{k}|\hat{h}_1\end{pmatrix}. \tag{B2}$$

At second order, one gets

$$\begin{aligned}u_x^{(2)}(\boldsymbol{k},z)=\bar{\delta}\frac{1+\nu}{1-\nu}\frac{e^{|\boldsymbol{k}|(z-h_0)}}{|\boldsymbol{k}|^3}\int d\boldsymbol{k}_1\frac{\hat{h}_1(\boldsymbol{k}_1)\hat{h}_1(\boldsymbol{k}-\boldsymbol{k}_1)}{|\boldsymbol{k}_1|}\\ \times\mathrm{i}\{k_x(z-h_0)|\boldsymbol{k}|[|\boldsymbol{k}||\boldsymbol{k}_1|\boldsymbol{k}\cdot\boldsymbol{k}_1-2(\boldsymbol{k}\cdot\boldsymbol{k}_1)^2\\ -2\nu(\boldsymbol{k}\wedge\boldsymbol{k}_1)^2]+(1-2\nu)k_x|\boldsymbol{k}||\boldsymbol{k}_1|\boldsymbol{k}\cdot\boldsymbol{k}_1\\ -4(1-\nu)[k_{1,x}|\boldsymbol{k}|^2\boldsymbol{k}\cdot\boldsymbol{k}_1+\nu k_x(\boldsymbol{k}\wedge\boldsymbol{k}_1)^2]\}\end{aligned} \tag{B3}$$

with a similar expression for $u_y^{(2)}$ after the exchange of x and y while $u_z^{(2)}$ is given by

$$\begin{aligned}u_z^{(2)}(\boldsymbol{k},z)=\bar{\delta}\frac{1+\nu}{1-\nu}\frac{e^{|\boldsymbol{k}|(z-h_0)}}{|\boldsymbol{k}|^3}\int d\boldsymbol{k}_1\frac{\hat{h}_1(\boldsymbol{k}_1)\hat{h}_1(\boldsymbol{k}-\boldsymbol{k}_1)}{|\boldsymbol{k}_1|}\\ \times\{(z-h_0)|\boldsymbol{k}|^2[2(\boldsymbol{k}\cdot\boldsymbol{k}_1)^2+2\nu(\boldsymbol{k}\wedge\boldsymbol{k}_1)^2-|\boldsymbol{k}|\\ \times|\boldsymbol{k}_1|\boldsymbol{k}\cdot\boldsymbol{k}_1]+2(1-\nu)\boldsymbol{k}^2|\boldsymbol{k}_1|\boldsymbol{k}\cdot\boldsymbol{k}_1-2(1-2\nu)|\boldsymbol{k}|\\ \times[(\boldsymbol{k}\cdot\boldsymbol{k}_1)^2+\nu(\boldsymbol{k}\wedge\boldsymbol{k}_1)^2]\}.\end{aligned} \tag{B4}$$

*Also at Ecole Centrale Marseille.

†jnaqua@ec-marseille.fr

‡thomas.frisch@im2np.fr

[1] I. N. Stranski and L. von Krastanow, Akad. Wiss. Lit. Mainz Abh. Math. Naturwiss. Kl. **146**, 797 (1939).

[2] A. Pimpinelli and J. Villain, *Physics of Crystal Growth* (Cambdrige University Press, Cambridge, 1998).

[3] V. A. Shchukin and D. Bimberg, Rev. Mod. Phys. **71**, 1125

(1999).
[4] P. Politi, G. Grenet, A. Marty, A. Ponchet, and J. Villain, Phys. Rep. **324**, 271 (2000).
[5] C. Teichert, Phys. Rep. **365**, 335 (2002).
[6] V. Shchukin, N. Ledentsov, and D. Bimberg, *Epitaxy of Nanostructures* (Springer, New York, 2003).
[7] J. Stangl, V. Holý, and G. Bauer, Rev. Mod. Phys. **76**, 725 (2004).
[8] I. V. Markov, *Crystal Growth for Beginners* (World Scientific, Singapore, 2004).
[9] J. Baribeau, X. Wu, N. Rowell, and D. Lockwood, J. Phys.: Condens. Matter **18**, R139 (2006).
[10] C. Misbah, O. Pierre-Louis, and Y. Saito, Rev. Mod. Phys. **82**, 981 (2010).
[11] M.-I. Richard, M. J. Highland, T. T. Fister, A. Munkholm, J. Mei, S. K. Streiffer, C. Thompson, P. H. Fuoss, and G. B. Stephenson, Appl. Phys. Lett. **96**, 051911 (2010).
[12] J. L. Gray, R. Hull, C.-H. Lam, P. Sutter, J. Means, and J. A. Floro, Phys. Rev. B **72**, 155323 (2005).
[13] Y. Tu and J. Tersoff, Phys. Rev. Lett. **98**, 096103 (2007).
[14] M. R. McKay, J. A. Venables, and J. Drucker, Solid State Commun. **149**, 1403 (2009).
[15] I. Berbezier and A. Ronda, Surf. Sci. Rep. **64**, 47 (2009).
[16] M. Brehm *et al.*, Phys. Rev. B **80**, 205321 (2009).
[17] P. Sutter and M. G. Lagally, Phys. Rev. Lett. **84**, 4637 (2000).
[18] R. M. Tromp, F. M. Ross, and M. C. Reuter, Phys. Rev. Lett. **84**, 4641 (2000).
[19] A. G. Cullis, D. J. Robbins, A. J. Pidduck, and P. W. Smith, J. Cryst. Growth **123**, 333 (1992).
[20] D. E. Jesson, S. J. Pennycook, J.-M. Baribeau, and D. C. Houghton, Phys. Rev. Lett. **71**, 1744 (1993).
[21] C. S. Ozkan, W. D. Nix, and H. Gao, Appl. Phys. Lett. **70**, 2247 (1997).
[22] I. Berbezier, B. Gallas, A. Ronda, and J. Derrien, Surf. Sci. **412-413**, 415 (1998).
[23] H. Gao and W. Nix, Annu. Rev. Mater. Sci. **29**, 173 (1999).
[24] J. A. Floro, E. Chason, L. B. Freund, R. D. Twesten, R. Q. Hwang, and G. A. Lucadamo, Phys. Rev. B **59**, 1990 (1999).
[25] R. J. Asaro and W. A. Tiller, Metall. Trans. **3**, 1789 (1972).
[26] M. A. Grinfel'd, Sov. Phys. Dokl. **31**, 831 (1986).
[27] J. A. Floro, M. B. Sinclair, E. Chason, L. B. Freund, R. D. Twesten, R. Q. Hwang, and G. A. Lucadamo, Phys. Rev. Lett. **84**, 701 (2000).
[28] I. Berbezier, A. Ronda, and A. Portavoce, J. Phys.: Condens. Matter **14**, 8283 (2002).
[29] I. Berbezier, A. Ronda, F. Volpi, and A. Portavoce, Surf. Sci. **531**, 231 (2003).
[30] D. B. Migas, S. Cereda, F. Montalenti, and L. Miglio, Surf. Sci. **556**, 121 (2004).
[31] G.-H. Lu and F. Liu, Phys. Rev. Lett. **94**, 176103 (2005).
[32] S. Balibar, H. Alles, and A. Y. Parshin, Rev. Mod. Phys. **77**, 317 (2005).
[33] S. Balibar, D. O. Edwards, and W. F. Saam, J. Low Temp. Phys. **82**, 119 (1991).
[34] P. Nozières, J. Phys. I **3**, 681 (1993).
[35] B. J. Spencer, S. H. Davis, and P. W. Voorhees, Phys. Rev. B **47**, 9760 (1993).
[36] W. H. Yang and D. J. Srolovitz, Phys. Rev. Lett. **71**, 1593 (1993).
[37] B. J. Spencer and D. I. Meiron, Acta Metall. Mater. **42**, 3629 (1994).
[38] K. Kassner and C. Misbah, Europhys. Lett. **28**, 245 (1994).
[39] Y. Pang and R. Huang, Phys. Rev. B **74**, 075413 (2006).
[40] M. S. Levine, A. A. Golovin, S. H. Davis, and P. W. Voorhees, Phys. Rev. B **75**, 205312 (2007).
[41] J.-N. Aqua, T. Frisch, and A. Verga, Phys. Rev. B **76**, 165319 (2007).
[42] J.-N. Aqua, T. Frisch, and A. Verga, Phys. Rev. E **81**, 021605 (2010).
[43] L. G. Wang, P. Kratzer, M. Scheffler, and N. Moll, Phys. Rev. Lett. **82**, 4042 (1999).
[44] C.-H. Chiu, Appl. Phys. Lett. **75**, 3473 (1999).
[45] Y. W. Zhang, Phys. Rev. B **61**, 10388 (2000).
[46] C.-H. Chiu, Phys. Rev. B **69**, 165413 (2004).
[47] P. Liu, Y. W. Zhang, and C. Lu, Appl. Phys. Lett. **88**, 041922 (2006).
[48] C.-H. Chiu and Z. Huang, Appl. Phys. Lett. **89**, 171904 (2006).
[49] C.-H. Chiu and Z. Huang, J. Appl. Phys. **101**, 113540 (2007).
[50] Z. Zhong, W. Schwinger, F. Schäffler, G. Bauer, G. Vastola, F. Montalenti, and L. Miglio, Phys. Rev. Lett. **98**, 176102 (2007).
[51] Y. Xiang and W. E, J. Appl. Phys. **91**, 9414 (2002).
[52] P. Liu, Y. W. Zhang, and C. Lu, Phys. Rev. B **68**, 035402 (2003).
[53] A. J. Pidduck, D. J. Robbins, A. G. Cullis, W. Y. Leong, and A. M. Pitt, Thin Solid Films **222**, 78 (1992).
[54] W. W. Mullins, J. Appl. Phys. **28**, 333 (1957).
[55] B. J. Spencer, P. W. Voorhees, and S. H. Davis, Phys. Rev. Lett. **67**, 3696 (1991).
[56] P. Müller and R. Kern, Appl. Surf. Sci. **102**, 6 (1996).
[57] M. J. Beck, A. van de Walle, and M. Asta, Phys. Rev. B **70**, 205337 (2004).
[58] A. A. Golovin, S. H. Davis, and A. A. Nepomnyashchy, Phys. Rev. E **59**, 803 (1999).
[59] H. R. Eisenberg and D. Kandel, Phys. Rev. Lett. **85**, 1286 (2000).
[60] Y. W. Zhang and A. F. Bower, Appl. Phys. Lett. **78**, 2706 (2001).
[61] A. Ramasubramaniam and V. B. Shenoy, J. Appl. Phys. **95**, 7813 (2004).
[62] Y. W. Zhang, Phys. Rev. B **60**, 13325 (1999).
[63] J. Tersoff, B. J. Spencer, A. Rastelli, and H. von Känel, Phys. Rev. Lett. **89**, 196104 (2002).
[64] A.-K. Kassam and L. N. Trefethen, SIAM J. Sci. Comput. (USA) **26**, 1214 (2005).
[65] The value of 8 ML layers is obtained using the method of stability analysis at zero flux and takes into account the surface rigidity for the (001) orientation.
[66] www.im2np.fr/pperso/aqua/films.html
[67] J. Tersoff and R. M. Tromp, Phys. Rev. Lett. **70**, 2782 (1993).
[68] We checked, by analyzing a model of two islands on a fixed wetting layer, that the surface energy difference between the (001) and (105) orientations is not too large so that there is no energy minimum which would correspond to two identical islands.